Nanoscale

PAPER

View Article Online
View Journal

Cite this: DOI: 10.1039/d5nr04427h

Ultracompact on-chip coiled waveguide-integrated photodetectors enabled by 2D materials with enhanced responsivity

Maaz Ahmed Qureshi, *†[a] Fooqia Khalid,†[b] Janvit Tippinit,[a] Faisal Ahmed,[b] Md Gius Uddin,[b] Abde Mayeen Shafi,[b] Xiaoqi Cui,[b] Matthieu Roussey,[a] Zhipei Sun,[b] Harri Lipsanen[b] and Markku Kuittinen[a]

High-performance on-chip photodetectors are critical for next-generation integrated photonic systems that enable efficient sensing, optical communication, and light detection. Waveguide-integrated two-dimensional (2D) materials, among various material platforms, offer promising solutions for enhanced light–matter interactions due to their remarkable electrical and optical properties. In this article, we have simulated and experimentally demonstrated, for the first time, an ultracompact MoS_2-based photodetector integrated with a coiled silicon nitride waveguide, which is designed to maximize the light–matter interaction by increasing the optical light absorption and improving the responsivity and external quantum efficiency. In contrast to the conventional straight waveguide integration with 2D materials, the coiled waveguide architecture with the MoS_2 flake significantly extends the optical interaction length, which allows prolonged evanescent interaction with the MoS_2 flake, resulting in an increase in responsivity of over 500% compared to a referenced straight waveguide structure. Our fabricated coiled structural photodetector achieves an excellent responsivity of 600 mAW^{-1}, an external quantum efficiency of 145%, a normalized photocurrent-to-dark current ratio of 9.35×10^{14} AW^{-3}, and a noise equivalent power of 1.72×10^{-9} W under optimal operating conditions. The coiled waveguide's performance confirms that this architecture maximizes optical absorption and photocurrent by extending the light–matter interaction length.

Received 21st October 2025,
Accepted 1st December 2025

DOI: 10.1039/d5nr04427h

rsc.li/nanoscale

1 Introduction

Integrated silicon photonics has transformed optoelectronics, energy-efficient computing, and high-speed communication networks, making it a revolutionary technology in information systems. Alongside this silicon-based development, silicon nitride (Si_3N_4) waveguides have emerged as one of the most promising platforms among the other photonic materials due to their low propagation loss, wide transparency window (400 nm to 5 μm), and compatibility with CMOS fabrication techniques.[1–3] Because of these characteristics, Si_3N_4-based photonic circuits are perfect for use in quantum photonics, nonlinear optics, sensing, and telecommunications.[4,5]

Different geometries are employed to enhance the interaction between light and materials within integrated photonic devices. Examples include straight waveguides, microring resonators, serpentine waveguides, and slow light photonic crystal waveguides.[6–9] While microrings and slow light photonic crystals can give strong enhancement, they typically exhibit narrowband and are susceptible to small fabrication errors or changes in wavelength.[10,11] Serpentine layouts can fit a long optical path into a small area, and ultrathin cores can improve the overlap with the active material.[12,13] However, both often require stricter process control and more complex fabrication.

Furthermore, new approaches for improving light–matter interactions, especially in photodetection applications, have been made possible by the integration of two-dimensional (2D) materials with Si_3N_4 waveguides.[14] Ultrathin, high-performance photodetectors that surpass conventional semiconductor-based devices have been made possible by the strong optical response and tunable electrical properties of 2D transition metal dichalcogenides (TMDCs), such as molybdenum disulfide (MoS_2).[15–19]

MoS_2, a widely studied TMDC, exhibits a tunable bandgap, transitioning from an indirect bandgap (1.2 eV) in its bulk form to a direct bandgap (1.9 eV) in its monolayer form, making it highly suitable for broad-spectrum photodetection.[20–23] Moreover, MoS_2 presents high carrier mobility, strong excitonic interactions, and efficient charge separation, which are essential for achieving high photo-

[a]Center for Photonics Sciences, University of Eastern Finland, 80100 Joensuu, Finland. E-mail: maaz.qureshi@uef.fi, markku.kuittinen@uef.fi
[b]Department of Electronics and Nanoengineering, Aalto University, Espoo, Finland. E-mail: faisal.ahmed@aalto.fi, zhipei.sun@aalto.fi
†Contributed equally.

current generation and a highly responsive photodetector.[16,24] Other photodetectors, such as graphene-based photodetectors, have been extensively explored, but their zero bandgap restricts the optical absorption and responsivity under intrinsic or undoped conditions,[25,26] whereas photodetectors based on MoS_2 have presented strong light absorption, improved responsivity, and enhanced photogating effects because of their high absorption coefficients and intrinsic energy bandgaps.[15,27] Recent studies have demonstrated that light absorption through the evanescent field coupling can be enhanced by integrating MoS_2 with the waveguide structures, improving responsivity by efficiently generating charge carriers for photodetection.[28–31]

Despite these benefits, MoS_2 integrated with conventional straight waveguides presents challenges with device fabrication as long 2D material flakes are complicated to exfoliate and transfer onto the straight waveguide surfaces. Thus, the optical interaction length in such straight waveguides is limited, which restricts the amount of light absorbed in the MoS_2 layers. In 2D integrated photodetectors, much of the flake is not effectively used: with a straight waveguide, the light–matter interaction is limited to the flake's available length, so performance mainly depends on finding longer flakes. To overcome these limitations, we designed and fabricated a coiled Si_3N_4 waveguide structure that can significantly increase the interaction length between the MoS_2 flake and the guided optical mode without demanding long 2D material flakes. In this design, we increase the effective interaction area so that more of the flake overlaps the guided mode, which extends the interaction length within the same device footprint and improves performance. The guided optical mode interacts with the MoS_2 layer over a much longer distance, enhancing the light–matter interaction, which results in better light absorption, increased photocurrent generation, and improved responsivity. Furthermore, the coiled architecture ensures that a higher percentage of the guided light interacts with the MoS_2 by enhancing evanescent field coupling, thereby improving overall device performance.

In this study, we compare and evaluate the performance of MoS_2-integrated photodetectors based on a coiled Si_3N_4 waveguide and its straight waveguide counterpart. By conducting waveguide engineering with 2D materials, we achieved enhanced light–matter interactions, improved responsivity, and photodetection efficiency. The results establish strong experimental validation for the superiority of coiled waveguides in 2D material-integrated photodetection and provide a platform for highly sensitive CMOS-compatible photonic devices for sensing, communication, and quantum photonic systems.

2 Design and simulations

In 2D materials, photodetection occurs through the photovoltaic and photoconductive effects, where incident light excites electron–hole pairs, altering the conductivity of the material and facilitating charge transport.[23,32,33] In waveguide-integrated photodetectors, light travels through the waveguide, and its evanescent field interacts with the 2D material, *e.g.*, the MoS_2 layer in our case, allowing for efficient light absorption and charge generation without the need for direct illumination from a free-space light source.[34] At the metal–MoS_2 junction, the alignment of energy levels (Fermi level) changes the electronic band structure, which affects how charges move, recombine, and contribute to the overall photodetection process.[35,36] To examine how the coiled waveguide-integrated MoS_2 photodetector performs, electrical and optical measurements were conducted under different light intensities and voltage conditions. Important figures of merit of photodetectors such as the photocurrent (I_{pc}), responsivity, external quantum efficiency (EQE), noise equivalent power (NEP), and normalized photocurrent-to-dark current ratio (NPDR) were evaluated to determine how the coiled waveguide design improves light absorption and charge collection efficiency. The results of the simulation of the designed device demonstrate that a significant portion of light is absorbed by the 2D material layered on the surface of the Si_3N_4 waveguide. This is further validated by experimental results, which show enhanced photocurrent generation and consequently higher responsivity due to the increased interaction length in the coiled waveguide configuration.

A straight Si_3N_4 waveguide is simulated in Fig. 1 to analyze the propagation of a transverse electric (TE) field in the waveguide. Fig. 1a shows a 3D schematic of the device, illustrating the device architecture with MoS_2 on the top surface of the waveguide. The evanescent field of the coupled light overlaps with the MoS_2 flake, which enables light absorption. In Fig. 1b, a cross-sectional view of the waveguide illustrates 95% of the optical mode confinement within the Si_3N_4 waveguide core, where the propagation of light occurs along the *z*-direction (into the plane of the page). The Si_3N_4 waveguide has a cross-sectional width of 1.3 μm and a thickness of 330 nm, and the same geometry was used in both the simulations and the fabricated device. Fig. 1c shows the mode profile when a 30 nm MoS_2 flake is integrated on top of the waveguide. The optical mode shifts upwards in the MoS_2 film, indicating an increase in light–matter interaction, leading to enhanced optical absorption in the film. The enhancement in evanescent field coupling is mainly due to the higher complex refractive index of the MoS_2 layer ($n_{MoS_2} \approx 4.15$, $k_{MoS_2} \approx 0.14$) compared to that of the Si_3N_4 waveguide ($n_{Si_3N_4} \approx 2.05$) at a wavelength of 532 nm. This causes the optical field to shift more into the MoS_2 flake, leading to stronger light–matter interaction. In the simulated straight configuration, approximately 17% of the guided light is confined within the film, highlighting the effectiveness of MoS_2 integration in enhancing responsivity. Fig. S1a in the SI shows the effect of varying the thickness of MoS_2 on the profile of the optical mode. Fig. S1(b and c) further discusses the optical mode confinement in the MoS_2 and attenuation in the Si_3N_4 waveguide core as the thickness of the top MoS_2 layer is varied from 0 to 30 nm. With an increase in the MoS_2 thickness, light absorption in the

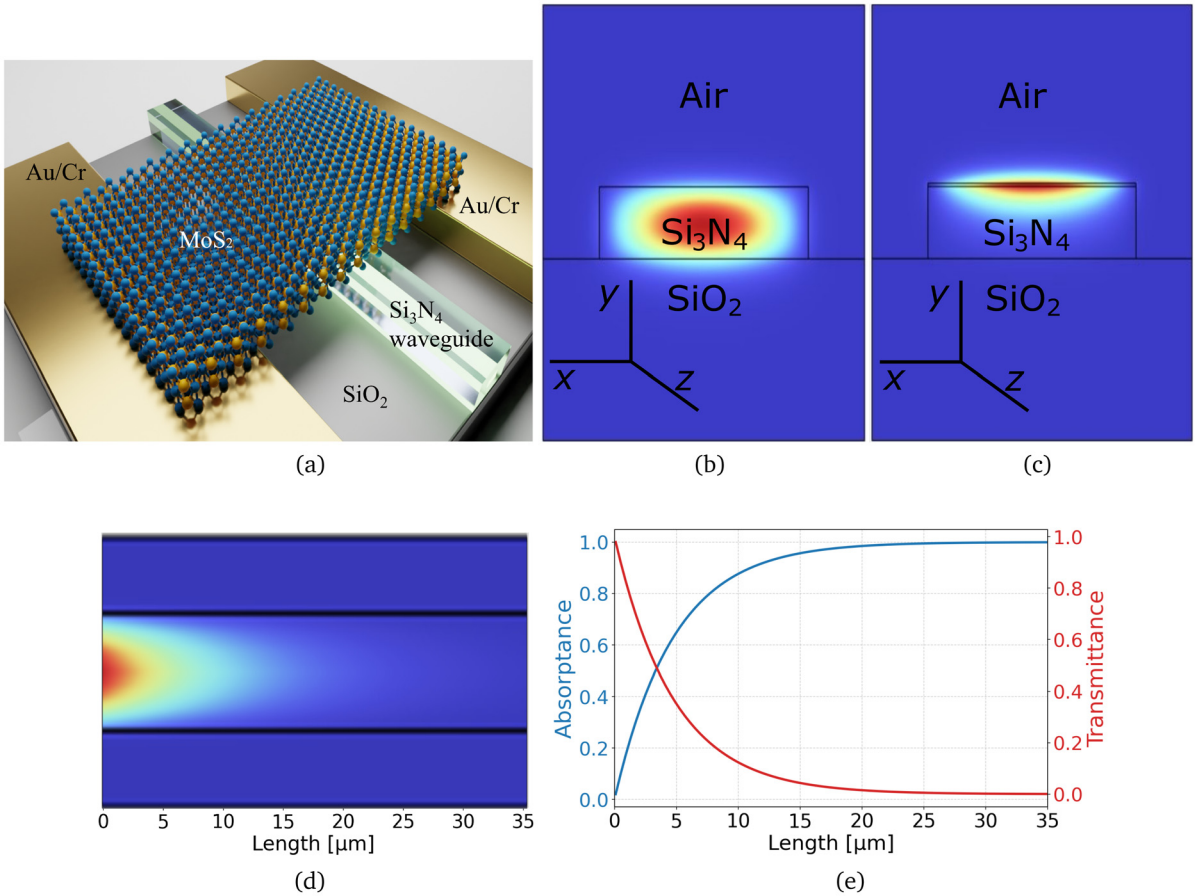

Fig. 1 Schematic and simulation results of the MoS_2-based photodetector on a Si_3N_4 waveguide. (a) Schematic representation of a straight waveguide integrated with the MoS_2 film, illustrating the integration of guided light with the 2D material. (b) A cross-sectional view of a bare Si_3N_4 waveguide shows that ~95% of the optical mode is confined in the waveguide core. (c) A cross-sectional view of a 30 nm thick MoS_2 film on the top surface of the Si_3N_4 waveguide shows that ~17% of the optical mode is confined in the MoS_2 film and ~61% in the Si_3N_4 core and surrounding, highlighting the strong light confinement in the film because of the film's higher refractive index. (d) Top-view simulated absorption map for a MoS_2-covered Si_3N_4 waveguide (geometry in panel (c)); light propagates along the waveguide axis. (e) Simulated absorption and transmission of the guided mode *versus* propagation length for the same structure, showing that lengths exceeding 25 μm are required to absorb nearly all guided power in the MoS_2 film.

material and the attenuation constant increase, and the optical mode becomes gradually more confined in MoS_2.

In Fig. 1d, the top view of a straight Si_3N_4 waveguide is simulated to illustrate light absorption within the MoS_2 film. The results suggest an efficient light–matter interaction and light absorption in the 30 nm thick MoS_2-integrated waveguides (cross-section shown in panel (c)), which emphasizes their suitability for photodetection applications.[23,37] In Fig. 1e, the relationship between absorption and transmittance as a function of film length for the same structure is further analyzed, indicating that over 25 μm of film length is required for the absorption to reach a significant level. This suggests that a relatively long MoS_2 flake is essential to absorb all the light. However, in most practical experimental conditions, finding, exfoliating, and transferring large-area 2D materials onto straight waveguides raise substantial fabrication challenges, which limit the feasibility of achieving long interaction lengths with strong responsivities. Consequently, a straight waveguide architecture may not entirely exploit the optical and electrical properties of MoS_2, which emphasizes the need for alternative waveguide architectures that can boost optical absorption while maintaining fabrication feasibility.

To address these limitations, we introduce and optimize a coiled Si_3N_4 waveguide architecture that extends the light–matter interaction length without requiring long MoS_2 flakes, as schematically illustrated in Fig. 2. A coiled Si_3N_4 waveguide design, unlike its straight waveguide counterpart, allows the guided mode to interact with the MoS_2 flake layer over a longer distance, effectively increasing the overall light absorption in the flake without increasing the actual size of the flake.[7,38–41] Our proposed hybrid photodetector design has the potential to significantly improve the carrier generation, responsivity, and overall photodetection response. Furthermore, to validate this hypothesis, we performed fabrication and measurements to experimentally confirm the predicted enhancements and optimize the coiled Si_3N_4 waveguide structural approach for the high-performance 2D material-based photodetector.

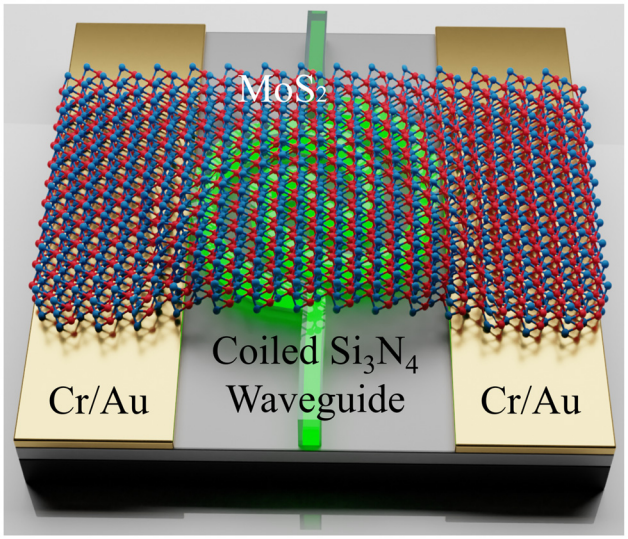

Fig. 2 3D schematic of the device: a MoS_2 flake bridges the Au/Cr source and drain electrodes on a substrate and overlies a coiled Si_3N_4 waveguide. The coiled geometry lengthens the guided-mode path and enhances light absorption within a compact footprint.

3 Photodetector measurements

We fabricated two photodetector configurations with exfoliated MoS_2 flakes transferred onto each waveguide structure, as detailed in sec. 5. The MoS_2 flakes are placed on the waveguide surface, and the devices are annealed under high temperature and vacuum conditions to improve the contact quality, remove fabrication processing-induced defects, and optimize charge transport. To simplify the fabrication process, particularly due to the need for long flakes, multilayer MoS_2 flakes were chosen over single-layer flakes for experimental implementation. Photodetection measurements are conducted using optical and electrical measurements. We used techniques such as Raman spectroscopy and atomic force microscopy (AFM) to analyze the structure and optical quality of the transferred MoS_2 flakes. The Raman results, shown in the SI, Fig. S2, were in agreement with previous studies,[42–44] confirming that the flakes are of good quality. AFM analysis, shown in SI Fig. S3, revealed that the MoS_2 flakes used for the experimental validation are multilayer flakes. These optical and structural characterization processes provide insights into the properties of the flakes used to fabricate the MoS_2-based waveguide integrated photodetectors.

3.1 Photodetector response with MoS_2 on a straight waveguide architecture

Fig. 3 presents the optical image and key optoelectronic characteristics of the straight waveguide photodetector. Fig. 3a is obtained with an optical microscope and shows a top view of the device with a MoS_2 flake integrated with a straight waveguide. The MoS_2 flake shown in the image has an estimated interaction length of 20 μm, facilitating light–matter interaction through lateral waveguide illumination, which leads to charged carrier generation. SI Fig. S3a shows that the thickness of the flake is approximately 30 nm. Fig. 3b presents the measured source–drain current (I_{sd}) as a function of the source–drain voltage (V_{sd}), *i.e.*, the current–voltage (I–V) characteristic of the device, under different illumination powers, with actual optical power (P_{opt}) levels ranging from 0.02 μW to 7.20 μW. The dark current measurements represented by the black reference curve show that illumination significantly increases the photocurrent, which is defined as the difference between the I_{sd} and the dark current. This demonstrates effective photon absorption and charge-carrier generation.

The waveguide characterization setup and the results of the transmission loss measurements of the Si_3N_4 waveguides are shown in SI Fig. S4. Optical power is coupled from the laser source to the tapered waveguide input through a butt-coupling technique as shown in SI Fig. S4(a and b). The transmission loss equation of our standard waveguide, shown in SI Fig. S4c, is utilized to estimate the actual optical power reaching the photodetector. The table in SI Fig. S4d compiles the power from the laser source output and the estimated actual power reaching the photodetector. The insertion and propagation losses of our standard waveguide are 12.09 dB and 1.05 dB cm^{-1}. The propagation losses are slightly higher due to fabrication imperfections, primarily from the sidewall roughness caused by reactive ion etching. These surface irregularities increase scattering losses in high-confinement Si_3N_4 waveguides.[45,46] Improving and further optimizing the etching and 2D material transfer steps should reduce both insertion and propagation losses. In addition, the optical reflections from the refractive index mismatch between the Si_3N_4 waveguide and the MoS_2 flake are suppressed by evanescent field coupling and uniform surface coverage, which also minimizes Fresnel losses.[47] Similar minimal back-reflection losses have also been observed in other waveguide-integrated 2D material photodetectors.[15,48,49]

The I–V curves shown in Fig. 3b, as well as the photocurrent shown in SI Fig. S5a, are plotted at various estimated actual power values ranging from 0.02 W to 7.20 W. Fig. S6a shows the measured dark current for MoS_2 flakes on a straight waveguide structure, indicating the actual scale of the current generated in the absence of illumination. These curves suggest a direct correlation between higher optical power levels and increased carrier generation. These electrical results confirm that the MoS_2 photodetector successfully detects incident light and provides stable optoelectronic functionality at varying input power intensities.

Responsivity (R) and external quantum efficiency (EQE) can be calculated as follows:

$$R = \frac{I_{pc}}{P_{opt}}[AW^{-1}]; \quad EQE = \frac{R \times h \times c}{q \times \lambda} \times 100[\%] \qquad (1)$$

where h = Planck's constant, c = speed of light, q = elementary charge, and λ = incident wavelength.

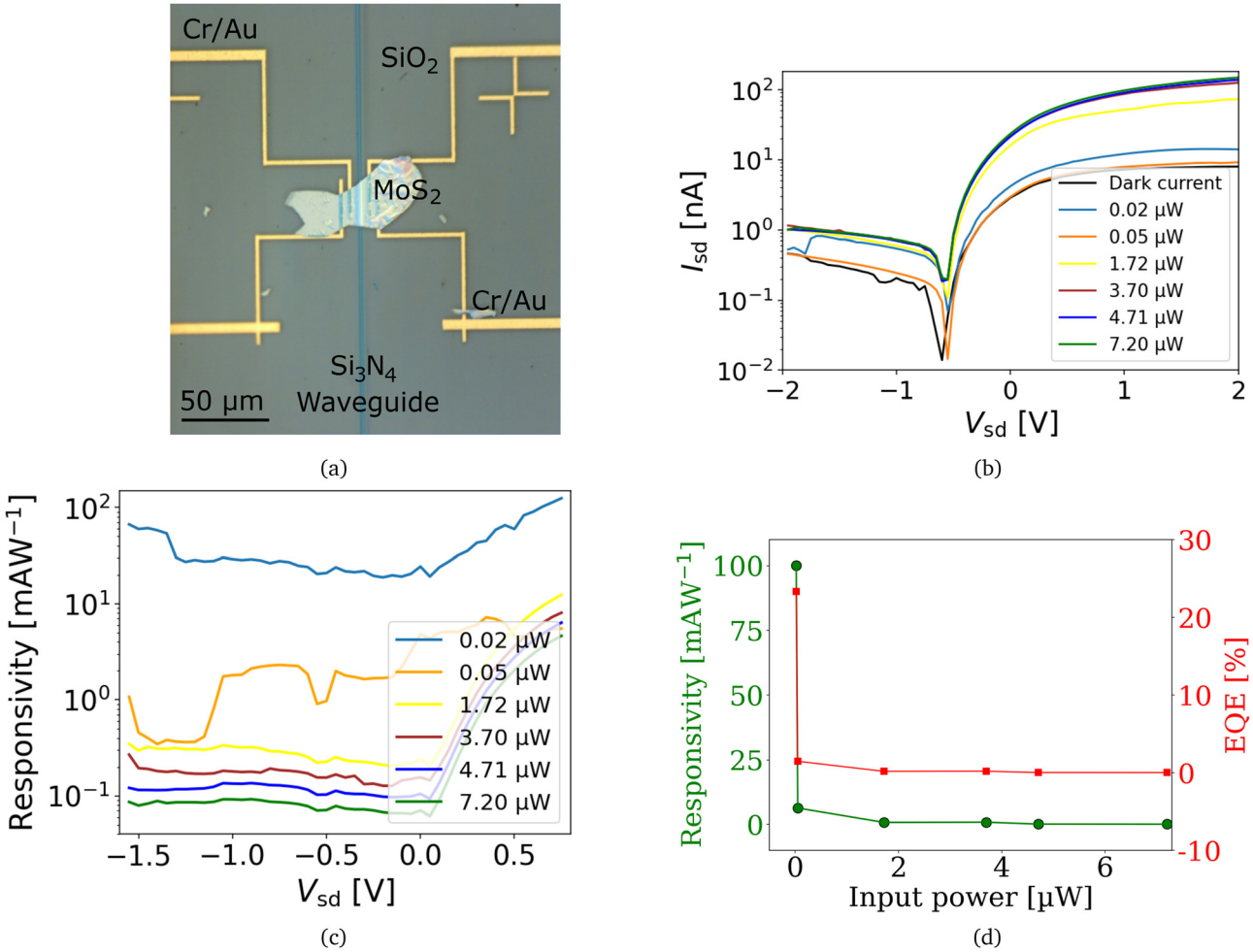

Fig. 3 Electrical characteristics and photoresponse of a MoS_2-based photodetector integrated with a straight Si_3N_4 waveguide with laterally incident light in a waveguide. (a) Optical microscopy image of the fabricated photodetector with a MoS_2 flake on the top surface of the straight waveguide. (b) Measured I–V characteristics and photocurrent generated under different illumination power levels, showing an increase in the photocurrent compared to dark conditions. (c) Responsivity as a function of V_{sd} in the device, revealing the influence of the bias voltage on the photodetection performance. (d) Responsivity and EQE dependence on input optical powers with laser light coupled laterally in the waveguide.

Here, responsivity measures the photocurrent output of a device per unit of incident optical power, whereas EQE quantifies how efficiently incident photons are converted into collected charge carriers. Both parameters are critical for determining the performance of a photodetector, with a high EQE ensuring minimal photon losses and a responsivity increasing with wavelength at a fixed EQE. The R and EQE results for the photodetector with MoS_2 on a straight waveguide are analyzed in Fig. 3c and d, respectively.

Fig. 3c plots the relationship of R as a function of V_{sd}, revealing notable fluctuations at different optical powers. The distinct drop in R, particularly at a low optical power (0.02 μW), indicates possible effects of charge trapping, carrier recombination, or interfacial defects, all of which reduce transport efficiency.[50,51] Fig. 3d shows the responsivity and EQE as a function of optical power levels, demonstrating a declining trend at higher levels, which is likely due to photocarrier saturation. This behavior, which restricts further improvements in responsivity occurs when excess carrier generation increases recombination rates, thus causing optical saturation.[15,52,53]

Overall, our measurements support effective MoS_2 photodetection with a straight waveguide under low illumination, resulting in a responsivity of about 100 mAW^{-1} at V_{sd} = −2 V and low illumination. Although the straight waveguide-assisted lateral light absorption improves photodetection performance, further enhancements in responsivity and light–matter interaction may be achieved by alternative waveguide architectures, such as micro-resonant, slow-light waveguides, and other photonic structures.[7,54] Such architectures can enhance light absorption and overall device responsivity; here we fabricate and present a coiled waveguide implementation.

3.2 Photodetector response with MoS_2 on a coiled waveguide architecture

Here, we fabricated a coiled waveguide structure and integrated it with MoS_2 to validate our hypothesis that elongated

interactions would improve light absorption in such structures. Fig. 4 presents the optical and electrical characterization of such a MoS_2-based coiled waveguide photodetector. Fig. 4a shows the top-view optical microscopy image of the MoS_2 flake transferred onto a coiled waveguide structure. SI Fig. S3b reveals that the thickness of the flake is 15 nm. As shown in Fig. 4a, the coiled waveguide photodetector has a minimum bend radius of 3 μm and provides an interaction length with the 2D flake of up to 200 μm, roughly ten times that of a straight waveguide. This photodetector was characterized using the method described in section 3.1. Again, the actual power reaching the photodetector is estimated using the loss transmission equation fitted from SI Fig. S4c.

Fig. 4b presents I_{sd} as a function of V_{sd} for illumination powers from 0.02 μW to 7.20 μW at 532 nm, showing a strong photocurrent enhancement. Fig. S6b shows the measured dark current for MoS_2 flakes on a coiled waveguide structure. Unlike the straight waveguides as discussed in section 3.1, the coiled waveguide structure has prolonged light absorption by increasing the interaction length, leading to higher charge carrier generation and charge collection. The photocurrent response of the device is further examined in SI Fig. S5b, confirming that higher optical power levels result in greater charge carrier generation. Notably, the photocurrent increase in the coiled waveguide is steeper than that in the straight configuration, emphasizing the enhanced light–matter interaction and improved photodetection performance.

Fig. 4c and d demonstrate that the coiled waveguide photodetector achieves a high responsivity exceeding 600 mAW^{-1} and an external quantum efficiency of over 145% at $V_{sd} = -2$ V and low illumination. The device highlights its remarkable improvement over conventional straight waveguide designs. The enhancement is driven mainly by the coiled geometry, which extends the guided-mode interaction length. By winding

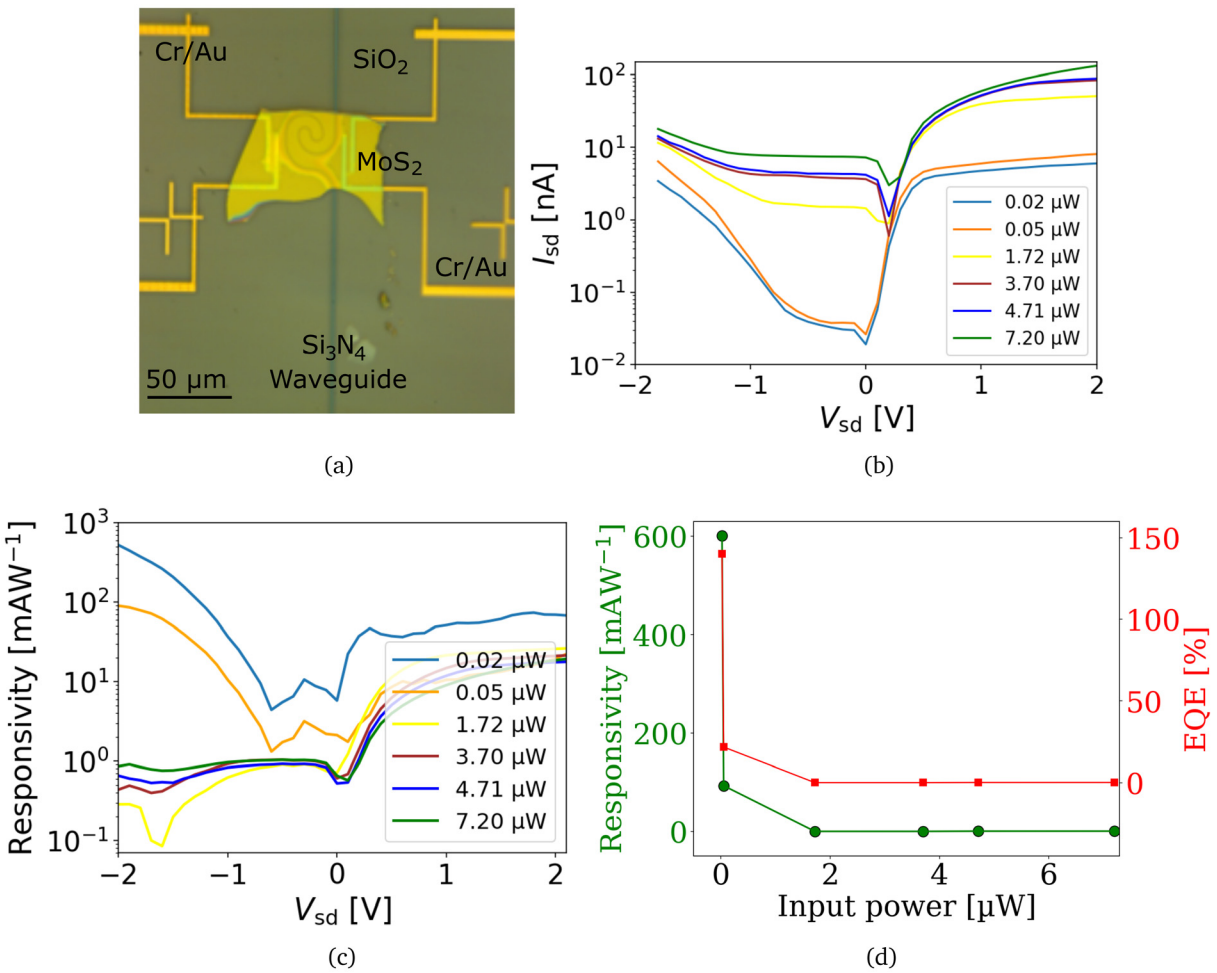

Fig. 4 Electrical *I–V* characteristics and photoresponse of a MoS_2-based photodetector integrated with a coiled Si_3N_4 waveguide structure with laterally incident light in the waveguide. (a) Optical microscopy image of the fabricated photodetector with a MoS_2 flake on the top surface of the coiled waveguide. (b) *I–V* characteristics and photocurrent generated under different illumination power levels, showing a significantly improved charge carrier generation. (c) Responsivity as a function of V_{sd} in the coiled waveguide device, revealing the influence of the bias voltage on the photodetection performance. (d) Responsivity and EQE dependence on input optical powers with light coupled laterally in the waveguide at a $V_{sd} = -2$ V.

the waveguide into a compact coil, the optical mode travels a longer path beneath the 2D flake, increasing cumulative absorption and the resulting photocurrent. In addition, the selected bend radius and waveguide cross-section shift the guided mode slightly toward the cladding where the 2D flake resides, increasing the mode's overlap with the film. Taken together, these effects boost performance without enlarging the device footprint.[54,55] Responsivity and EQE as a function of input optical powers are examined in Fig. 4d, showing a similar decreasing trend in responsivity at higher power levels, consistent with photocarrier saturation effects.[15,52,53] However, despite this decline, significantly higher overall responsivity and EQE are achieved with the coiled waveguide structure, demonstrating greater efficiency in detecting optical signals across a wide range of illumination intensity levels.

The Noise Equivalent Power (NEP) and Noise Power Detection Ratio (NPDR) are calculated as follows:

$$\mathrm{NEP} = \frac{I_{\mathrm{noise}}}{R}\,[\mathrm{W}]; \quad \mathrm{NPDR} = \frac{R}{\mathrm{NEP}^2}\,[\mathrm{AW}^{-3}] \tag{2}$$

Here, the NEP represents the minimum incident optical power at which the photodetector's signal equals its noise level, defined as a fundamental sensitivity limit. The NPDR evaluates a photodetector's ability to distinguish weak optical signals from dark current noise, indicating its signal-to-noise performance.

Fig. 5 shows the results of these calculations as a function of V_{sd}, demonstrating the excellent performance of the MoS_2-based photodetector integrated with a coiled waveguide structure. The results reveal a low NEP of less than 25 nW over the optimum bias range of V_{sd} from −2 V to 0 V, with a sharp NEP minimum of 1.72 nW at V_{sd} = −0.4 V, where the applied field enhances responsivity with a minimal increase in the dark current. The low range of NEP values indicates the remarkable sensitivity and ability to detect extremely weak optical signals. In addition, the device also achieves its peak detection capability with an NPDR of 8.10 × 10^{14} AW^{-3} at V_{sd} = −0.4 V, highlighting a critical operating point for ultra-low-power photodetection applications. The NEP dip and NPDR peak at V_{sd} = −0.4 V indicate an optimal operating bias point with a low dark current and efficient carrier extraction where the detection sensitivity is enhanced.[56–58] The bias-dependent behavior is typical in 2D materials due to the field-enhanced separation and suppressed recombination. Furthermore, the NPDR curve validates the superior performance of the photodetector, with the values exceeding 9.5 × 10^{14} AW^{-3} at V_{sd} = −1.9 V. The high NPDR values in the optimal biasing range, a highly desirable feature for optical sensors and imaging, confirm that the photodetector maintains outstanding signal distinction across a wide range of illumination intensities.

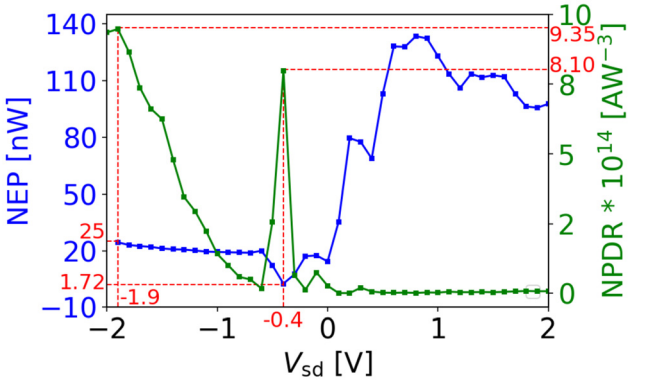

Fig. 5 Noise Equivalent Power (NEP) and Noise Power Detection Ratio (NPDR) of the MoS_2-based photodetector integrated with a coiled Si_3N_4 waveguide structure. The NEP (blue curve) and NPDR (green curve) are plotted as functions of V_{sd} to evaluate the device's performance and sensitivity. A minimum NEP value of +1.72 nW (indicating good performance) and a sharp peak in the NPDR are observed near V_{sd} = −0.4 V, suggesting an optimal operating point for low-noise detection. The NPDR reaches its maximum value of 9.35 × 10^{14} AW^{-3} at V_{sd} = −1.9 V, indicating enhanced photodetection capabilities under these biasing conditions.

For the coiled MoS_2 photodetector we estimate the electronic speed limits from the measured dark IV curve (Fig. S6b) and the transfer characteristics in Fig. S7. These give a gate-dependent source–drain resistance $R_{sd}(V_g)$ in the range $R_{sd} \approx (2–7) \times 10^8\ \Omega$ at V_{sd} = 4 V. The MoS_2 region between the contacts covers roughly 30 μm × 50 μm on top of a ~3 μm thick SiO_2 layer, corresponding to a total device capacitance of $C_{tot} \approx \varepsilon_0\varepsilon_r A/d \sim 2 \times 10^{-14}$ F (about 20 fF). This yields an RC time constant $\tau_{RC} \approx R_{sd}C_{tot}$ ~4–14 μs and an electrical bandwidth $f_{3dB} \approx 1/(2\pi\tau_{RC})$ ~10–40 kHz. Using the extracted effective mobility of the coiled device, $\mu_{FE} \approx 1.6 \times 10^{-2}$ $cm^2\ V^{-1}\ s^{-1}$, and the channel length $L \approx 30$ μm at V_{sd} = 4 V gives a carrier transit time:

$$t_{tr} \approx \frac{L^2}{\mu_{FE} V_{sd}} \approx 140\,\mu s,$$

corresponding to a transit-time-limited bandwidth f_{tr} ~1 kHz. These values are modest compared to the MHz–GHz bandwidths reported for optimized waveguide-integrated van der Waals photodetectors with engineered low-resistance contacts and extremely low capacitances.[59,60] This is consistent with the relatively long (~30 μm) channel and the extremely thick (~3 μm) SiO_2 back-gate dielectric, which yields a small gate capacitance, and the non-optimised contact resistance and trap density in the present geometry. These aspects are not fundamental to the coiled Si_3N_4 platform and could be improved in future designs by reducing the MoS_2 source–drain channel length, engineering lower-resistance contacts, reducing the pad area, and using a thinner or high-κ gate dielectric.

Waveguide propagation and dispersion are not expected to impose any additional speed limitations for the presented coiled design. The total interaction length of the MoS_2 flake on top of the Si_3N_4 waveguide is approximately $L_{wg} \approx 140$ μm. Using the speed of light under vacuum as an upper bound for the group velocity yields a photon transit time:

$$\tau_{ph} \gtrsim \frac{L_{wg}}{c} \approx 0.5\,ps.$$

This is more than five orders of magnitude shorter than the microsecond-scale RC and transit times estimated above. Over

an interaction length of only ~140 μm any dispersion-induced temporal broadening is negligible on this timescale, so the ultimate speed of the present coiled photodetectors is governed by electronic factors (RC constants, trap-assisted dynamics and effective mobility). Consequently, the coiled Si_3N_4 waveguide does not impose a fundamental dispersion-related bottleneck.

For MoS_2-based photodetectors, the coiled waveguide architecture offers higher responsivity and improved light absorption compared to conventional straight designs. The extended optical interaction length in this configuration significantly boosts carrier generation efficiency, making it well suited for low-power optical sensing, quantum optoelectronics, and integrated photonics. In addition, the compact structure exhibits an ultra-low NEP and a high NPDR within an optimal operating range, surpassing many other 2D material-based photodetectors.[61] Its ability to achieve strong light absorption while being readily integrated on-chip underscores its potential for advanced sensing technologies.[62] These results position the coiled waveguide design as a highly promising compact photodetector for next-generation photonics applications.

3.3 Architecture comparison and justification of enhanced optical response

Comparing the coiled and straight waveguide configurations shows that the coiled waveguide structures significantly improve optical absorption and responsivity. The responsivity is compared in Fig. 6. The analysis of experimental measurements revealed that the photodetector based on MoS_2 on a coiled waveguide structure demonstrated a ten times longer interaction length compared to the straight waveguide structure, leading to an improvement in photocarrier generation and efficiency. While the responsivity in the coiled waveguide configuration exceeded 600 mAW^{-1} at a V_{sd} of −2 V, it remained lower, below 100 mAW^{-1}, in the straight waveguide structure primarily due to the shorter optical path. Thus, we observed an increase in responsivity of over 500% in the coiled waveguide configuration where the optical path is folded in a confined geometry. The higher photocurrent noticed in the coiled waveguide device can be credited to the prolonged light–matter interaction that ensures a high percentage of incident photons contributing to the generation of charge carriers.

Although factors such as material thickness, contact resistance, and material quality can still influence the photocurrent and responsivity of the two MoS_2-based photodetectors discussed, the significant increase in responsivity observed in the coiled waveguide-based device is likely attributable to the waveguide geometry, as other performance-affecting parameters were kept as consistent as possible. Typically, thicker MoS_2 flakes tend to exhibit higher photocurrent generation due to higher absorption. Yet, in our measurements, the coiled waveguide structure with a thinner MoS_2 flake demonstrated superior photocurrent and responsivity, thanks to the longer optical interaction length, highlighting the effectiveness of the geometry in enhancing the interaction between light and matter.[68,69] Similar geometric optimization strategies have

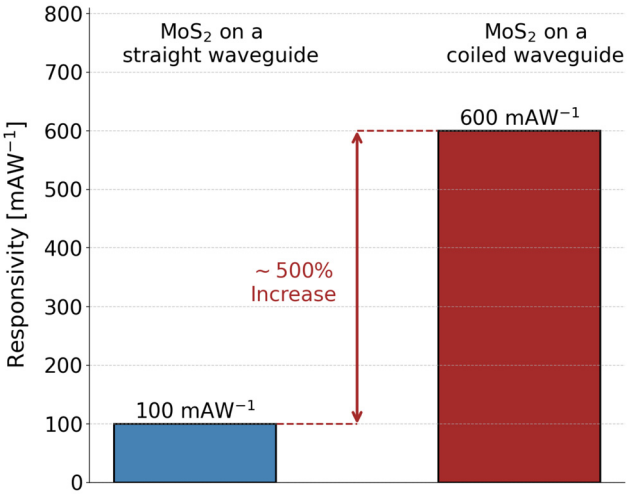

Fig. 6 Comparison of responsivity for MoS_2-based photodetectors integrated with conventional straight and novel compact coiled Si_3N_4 waveguide architectures. The photodetector integrated with a straight waveguide exhibits a responsivity of 100 mAW^{-1}, whereas the compact coiled waveguide-integrated photodetector demonstrates a substantially enhanced responsivity of 600 mAW^{-1}, signifying a 500% increase. This significant improvement in photodetection responsivity is attributed to the extended optical interaction length and enhanced light–matter interaction in the coiled waveguide structure.

demonstrated enhanced light absorption and improved performance in integrated 2D photonic devices.[54,70–73]

To further assess the effectiveness of a compact coiled waveguide design for enhancing light–matter interaction in ultra-thin 2D materials, we simulated the optical response of a Si_3N_4 waveguide paired with a monolayer MoS_2 film in SI Fig. S8. SI Fig. S8a shows the optical mode profile, revealing that the optical field is primarily confined within the Si_3N_4 core, with only a minor fraction evanescently coupling into the MoS_2 layer. SI Fig. S8b demonstrates this interaction, indicating that a propagation length of over 400 μm is required to achieve almost all of the optical absorption in the ultra-thin material. SI Fig. S8c shows the top-view simulation, visualizing the gradual attenuation of the optical field along the waveguide. These results further emphasize the significance of extended light–matter interaction lengths when working with atomically thin 2D materials and highlight the critical benefit of coiled waveguide designs, which enable long interaction paths in a limited chip area and reduce the challenges of exfoliating and transferring large-area monolayer films.

In the fabricated devices, the straight waveguide is covered by a ~30 nm MoS_2 flake, whereas the coiled waveguide uses a thinner ~15 nm flake. Eigenmode simulations at 532 nm (SI Fig. S9a and b) show that, for the experimental flake lengths, the total absorptance in the 15 nm coiled device (≈99.9%) is essentially the same as, and slightly higher than, that of the 30 nm straight device (≈99.3%). This indicates that the coiled geometry compensates for the smaller thickness by providing a longer interaction length and higher total optical absorption, consistent with the experimentally observed ~5× increase in

Table 1 Representative waveguide-integrated devices using different geometries to enhance performance

Material	Geometry	Performance	Remarks	Ref.
MoS_2/Si_3N_4	Coiled waveguide	$R \approx 600$ mAW^{-1}, EQE >140%	Compact, long interaction	This work
MoS_2/Si_3N_4	Straight waveguide	$R \approx 100$ mAW^{-1}	Straight reference	This work
$PtSe_2$/Si	Racetrack microring	High effective absorption	Ultra-compact, narrowband resonance	8
$PtSe_2$/Si	Ultra-thin straight waveguide	Enhanced mid-IR absorption	Broadband, thin core	6
Rb vapour/Si_3N_4	Serpentine waveguide	Strong coupling, low power	Serpentine, compact	63
SiO_2/Si	Serpentine waveguide	Loss ≈0.4–0.7 dB cm^{-1}	Serpentine, long path	64
BP/Si PhCWG	Slow-light PhC waveguide	$R \sim 11$ AW^{-1} (mid-IR)	Slow-light enhanced	65
Graphene/Si PhC WG	Slow-light PhC waveguide	mAW^{-1}-level R, bandwidth >5 GHz	High-speed graphene PD	66
Si PhC WG	Slow-light PhC waveguide	High R, GHz, low dark current	Si slow-light PD	67

responsivity. The same simulations also allow us to isolate the role of geometry at fixed MoS_2 thickness. For monolayer MoS_2 (0.65 nm), the calculated absorptance increases from 11.9% for the straight waveguide to 82.8% for the coiled waveguide, *i.e.* about a sevenfold gain purely due to the coiled layout. In this ultrathin regime, the extended interaction length provided by the coil therefore becomes even more important for achieving high absorption in a compact footprint and would be expected to translate into a correspondingly higher external responsivity if similar internal quantum efficiency is maintained. Together, these results show that the coiled waveguide geometry, rather than the difference in MoS_2 thickness alone, is the main driver of the enhanced optical absorption and hence the improved photodetector performance.

As summarised in Table 1, our coiled MoS_2/Si_3N_4 device provides a distinct trade-off between performance and fabrication complexity. The coiled waveguide achieves a responsivity of about 600 mAW^{-1} and an EQE above 140%, which is around five times higher than that of our straight-waveguide reference. Yet it is fabricated using standard Si_3N_4 waveguides, conventional lithography and a simple flake-transfer step. In contrast, micro-ring and slow-light photonic crystal devices in the literature can achieve very strong enhancement or high speed, but they rely on carefully tuned resonances and stricter fabrication control.[8,66] Ultra-thin and serpentine waveguides also require specialized processing to maintain low loss over long paths. These factors make the coiled waveguide a compact and comparatively easy-to-fabricate option for extending the propagation length of light in photodetectors.

Previous studies have shown that extending the propagation length of guided light within a 2D material generally increases light–matter interaction and responsivity by orders of magnitude.[54,74] In line with these findings, we have developed a new photodetector platform incorporating coiled Si_3N_4 waveguides. The results confirm that this architecture can significantly enhance photodetection performance by enabling prolonged interaction between light and the active material. This increases the potential for enhanced electron–hole pair generation upon photon absorption.[72] A benchmark table is included in SI Fig. S10 that compares the device performance of our coiled waveguide photodetector with the prior reported devices. The results of this study emphasize the superiority of a 2D material-based coiled waveguide over the conventional straight structure with better photodetection performance and a more compact footprint, allowing integration on-chip for the next generation, highly sensitive quantum and optoelectronic photonic devices.[73]

The main goal of this work was to demonstrate a highly sensitive photodetector with improved responsivity and external quantum efficiency using 2D materials integrated with waveguides. Our MoS_2-based photodetectors in a coiled waveguide structure exhibited low noise and high sensitivity. However, a limitation of this study is the absence of time-resolved measurements. Due to system constraints, we could not directly evaluate properties such as speed, rise time and fall time, but these will be important to study in future work.

The responsivity and EQE values reported in this work correspond to one fully characterised coiled device and its straight waveguide reference, fabricated on the same chip and measured under identical conditions. These devices were selected because they show clean contacts and complete MoS_2 coverage, and we consider them representative of the behaviour expected from the given geometry and process flow. Due to fabrication and time constraints, we did not perform a full statistical study over multiple identical samples. However, our simulations and design analysis show higher light absorption in the coiled structure, particularly for thin or monolayer MoS_2, which is consistent with the experimentally observed enhancement. Since this enhancement is mainly determined by the increased interaction length of the coiled geometry compared to the straight waveguide, we expect a similar improvement in responsivity for additional devices fabricated with the same design and process. A detailed variability study is left for future work.

4 Conclusions

This article demonstrates the first successful integration of a MoS_2-based photodetector on a compact coiled Si_3N_4 waveguide architecture, achieving an effective ten-fold increase in optical interaction length compared to the conventional straight waveguide structures. The coiled waveguide-based photodetector exhibits a remarkable responsivity exceeding 600 mAW^{-1} at a V_{sd} of −2 V, significantly outperforming MoS_2-based photodetectors on straight waveguides. In addition, the

device revealed an impressive NEP of 1.72 nW, an NPDR of 9.35×10^{14} AW^{-3}, and an EQE of 145% in the optimal biasing voltage range, allowing operation over a wide range of optical power levels. These theoretical and experimental findings confirm that coiled Si_3N_4 waveguides are an efficient and suitable platform for photodetectors based on 2D materials. This opens up the possibility of creating high-performance, low-power, and ultracompact optoelectronic devices for applications in sensing, communications, and quantum photonic technologies.

5 Device fabrication, materials and characterization

5.1 Device fabrication process

A 525 μm thick p-type silicon (Si) wafer with a <100> orientation is coated with a 3 μm wet thermal oxide layer and a 330 nm stoichiometric Si_3N_4 layer by low-pressure chemical vapor deposition (LPCVD). First, electron-beam lithography (EBL) is employed to pattern alignment markers using a positive photoresist (AR-672), followed by the development process, chromium and gold deposition, and a standard lift-off process. Alignment markers are used in the subsequent lithographic processes to precisely pattern waveguides and metal contacts on the same sample.

For waveguide patterning, the sample is cleaned with O_2 plasma for 2 minutes, and then a negative nLOF photoresist is spin-coated at 2000 rpm for 60 seconds to achieve a resist thickness of 500 nm on the Si_3N_4 sample. The sample is subsequently baked at 110 °C for 60 seconds. An EBL patterns the desired waveguide design on the resist, followed by the development and baking. The sample is then subjected to reactive ion etching (RIE) with CHF_3/O_2 gas mixtures to etch the Si_3N_4. The samples undergo an additional cleaning with O_2 plasma for 3 minutes to remove any residual contaminants. The fabricated structures are 0.33 μm thick and 1.3 μm wide, forming a low-loss waveguide.

To conduct electrical characterization, the sample undergoes another lithographic process to fabricate metal contacts close to the waveguide structures. The sample is spin-coated using a positive photoresist, followed by EBL-patterning, development, metal-deposition (2 nm Cr adhesion layer/50 nm Au) *via* physical vapor deposition (PVD), and successive lift-off processes. Finally, the sample is manually cleaved at the waveguide edges, enabling optical modes to couple *via* the butt-coupling method. In this method, a fiber-coupled laser is used to inject light into the waveguide. The typical measured length of the waveguides after cleaving the sample is approximately 1 cm, ensuring efficient optical transmission and device characterization.

The chips were manually cleaved perpendicular to the waveguide propagation direction so that the waveguide cross sections were exposed. For the photodetector experiments, we only used waveguides whose cleaved cross sections appeared clean and uniform under SEM. The coiled and straight devices reported here are located on the same cleaved chip and share the same input–output coupling conditions. Therefore, the variability in the cleaving process does not affect the comparison of their relative performances. Furthermore, by using the transmission equation described in SI Fig. S4c, we can estimate the actual optical power reaching the active MoS_2 region in both the coiled and straight waveguide cases. This effectively removes the influence of coupling and propagation losses when comparing responsivities.

5.2 Material exfoliation and transfer process

The sequential transfer process follows the method described by Kinoshita *et al.*[75] Bulk MoS_2 crystals from a 2D semiconductor are first exfoliated using the Scotch tape method, and the exfoliated flakes are picked up onto a PDMS stamp for later use. The PDMS is a commercially available sheet (Part No. PF-40 × 40-0170-X4, PF Film Series, 4″ × 4″, 17 mil) from GelPak, corresponding to a PDMS layer thickness of 430 μm. Using a pre-fabricated film with fixed composition and thickness ensures a well-defined stamp stiffness and minimizes device-to-device variability associated with the transfer medium.

Poly(propylene carbonate) (PPC) is used as a sacrificial layer to allow controlled transfer of MoS_2 flakes onto the waveguides. PPC is dissolved in anisole to form a 3% (by weight) solution, which is stirred at 60 °C for 24 h and then briefly heated to 70 °C to dissolve any remaining solid. The solution is spin-coated onto glass slides at 2000 rpm for 1 min and baked at 150 °C for 30 s. The PPC-coated slide is pressed onto the PDMS stamp carrying MoS_2 flakes and then lifted away, leaving flakes on the PPC layer. Suitable MoS_2 lakes are located under an optical microscope and aligned with the Si_3N_4 waveguide and metal contacts using a 2D-material transfer stage, with PDMS providing mechanical support; during this step the sample is held at 60 °C to soften the PPC and aid the release of the MoS_2 flakes. After the flake is placed, the sample is annealed at 180 °C for a few minutes to improve adhesion and remove contaminants. In our fabrication line, MoS_2 and related 2D-material devices are routinely annealed in the 150–250 °C range without observable degradation in Raman or optical response, so 180 °C was chosen as a conservative temperature that remains well within the tolerance of the material system while still providing efficient cleaning. Finally, the PPC is removed by immersion in acetone for 3 min, followed by rinsing with isopropanol and drying with nitrogen.

5.3 Electrical and optical characterization

The fabricated MoS_2-based waveguide integrated photodetector was optically and electrically characterized by placing the sample onto a printed circuit board (PCB), where the metal pads of the PCB are connected with the Cr/Au metal contacts to establish electrical connections. The resultant device was then mounted on the waveguide characterization setup stage, where a laser light at 532 nm wavelength was injected into the tapered Si_3N_4 waveguide (cross-section width of 3 μm at the waveguide input) using a butt-coupling technique.

Electrical characterization was conducted using Keithley 2400 and 2401 Source Meter Units (SMUs) to measure the I_{sd} as a function of V_{sd} under illuminated and dark conditions. The power of input laser light was systematically increased in order to measure the electro-optical response of the photodetector, and the corresponding *I–V* characteristics were recorded to analyze the dependence of photocurrent generation on the optical power.

To determine the actual power reaching the MoS_2 photodetector, the output power from the fiber-coupled laser was measured, and the transmission loss equation of the standard waveguide in our sample was applied to estimate the actual power reaching the active region of the fabricated photodetector. To measure the photocurrent generation and determine the responsivity of the device, the electrical response under both dark and illuminated conditions was recorded while the actual power reaching the photodetector was varied from 0.02 μW to 7.20 μW. All measurements were conducted at room temperature and pressure, and the data acquisition was automated using a customized LabVIEW program to ensure repeatability and high accuracy of the measurement process.

Author contributions

M. Q. conceived the project under the guidance of M. K., and M. R. Simulations of optical mode propagation in waveguides were performed by J. T. The samples were fabricated by M. Q. and F. K., who also performed the optoelectronic measurements. M. Q. performed the data analysis and drafted the manuscript in collaboration with F. K., J. T., F. A., G. U., A. S., X. C., M. R., Z. S., H. L., and M. K. All the authors have reviewed the manuscript.

Conflicts of interest

There are no conflicts to declare.

Data availability

Data for this article are available at Zenodo (Publisher) at https://doi.org/10.5281/zenodo.17403949.

Details of MoS_2 thickness-dependent simulations, Raman and AFM characterization, Si_3N_4 waveguide characterization, additional dark/photocurrent and transfer curves, simulated absorptance in straight and coiled geometries, and benchmarking against previous 2D-material waveguide photodetectors. See DOI: https://doi.org/10.1039/d5nr04427h.

Acknowledgements

We acknowledge the support and facilities provided by the University of Eastern Finland, Aalto University, Micronova Nanofabrication Center, and the funding provided by the Research Council of Finland grants (PREIN Flagship decision numbers 346518, 346529, and decision number 358812).

References

1 J. Liu, G. Huang, R. N. Wang, J. He, A. S. Raja, T. Liu, N. J. Engelsen and T. J. Kippenberg, *Nat. Commun.*, 2021, **12**, 2236.
2 A. L. Gaeta, M. Lipson and T. J. Kippenberg, *Nat. Photonics*, 2019, **13**, 158–169.
3 S. Romero-García, F. Merget, F. Zhong, H. Finkelstein and J. Witzens, *Opt. Express*, 2013, **21**, 14036–14046.
4 M. A. Kats, R. Blanchard, P. Genevet and F. Capasso, *Nat. Mater.*, 2013, **12**, 20–24.
5 D. J. Moss, R. Morandotti, A. L. Gaeta and M. Lipson, *Nat. Photonics*, 2013, **7**, 597–607.
6 T. Xu, L. Qi, Y. Xu, S. Xiao, Q. Yuan, R. Niu, J. Wang, H. K. Tsang, T. Liu and Z. Cheng, *Nanoscale*, 2024, **16**, 3448–3453.
7 X. He, Y. Wang, Z. Peng, Z. Li, X. Yu, L. Xu, X. Huang, X. Meng, W. Shi, X. Gao, *et al.*, *J. Mater. Chem. C*, 2024, **12**, 2279–2316.
8 T. Xu, Q. Yuan, S. Xiao, T. Liu, H. K. Tsang and Z. Cheng, *ACS Appl. Mater. Interfaces*, 2025, **17**, 24071–24078.
9 Z. Cheng, R. Guo, J. Wang, Y. Wang, Z. Xing, L. Ma, W. Wei, Y. Yu, H. K. Tsang and T. Liu, *Natl. Sci. Open*, 2022, **1**, 20220022.
10 A. Kotb, A. Hatziefremidis and K. E. Zoiros, *Nanomaterials*, 2025, **15**, 1736.
11 F. Chen, H. Xue, Y. Pan, M. Wang, Y. Hu, L. Zhang, Q. Chen, S. Han, G.-g. Liu, Z. Gao, *et al.*, arXiv, 2022, preprint, arXiv:2208.07228, DOI: 10.48550/arXiv.2208.07228.
12 L. Stern, B. Desiatov, N. Mazurski and U. Levy, *Nat. Commun.*, 2017, **8**, 14461.
13 S. Kim, C. Hong, Y. Chung, S. Kwon, S. Park, G. Baek, S. Woo, E. Kim and M. Lee, *Nano Lett.*, 2025, **25**, 14066–14073.
14 M. A. Qureshi, F. Khalid, M. G. Uddin, A. M. Shafi, I. Doughan, J. Tippinit, F. Ahmed, X. Cui, M. Roussey, H. Lipsanen and M. Kuittinen, *Nanoscale Adv.*, 2025, **7**, 7352–7362.
15 F. Koppens, T. Mueller, P. Avouris, A. Ferrari, M. S. Vitiello and M. Polini, *Nat. Nanotechnol.*, 2014, **9**, 780–793.
16 K. F. Mak and J. Shan, *Nat. Photonics*, 2016, **10**, 216–226.
17 L. Britnell, R. M. Ribeiro, A. Eckmann, R. Jalil, B. D. Belle, A. Mishchenko, Y.-J. Kim, R. V. Gorbachev, T. Georgiou, S. V. Morozov, *et al.*, *Science*, 2013, **340**, 1311–1314.
18 M. Turunen, M. Brotons-Gisbert, Y. Dai, *et al.*, *Nat. Rev. Phys.*, 2022, **4**, 219–236.
19 S. Manzeli, D. Ovchinnikov, D. Pasquier, *et al.*, *Nat. Rev. Mater.*, 2017, **2**, 17033.
20 O. Lopez-Sanchez, D. Lembke, M. Kayci, A. Radenovic and A. Kis, *Nat. Nanotechnol.*, 2013, **8**, 497–501.
21 K. S. Kim, Y. J. Ji, K. H. Kim, *et al.*, *Nat. Commun.*, 2019, **10**, 4701.

22 A. Splendiani, L. Sun, Y. Zhang, T. Li, J. Kim, C.-Y. Chim, G. Galli and F. Wang, *Nano Lett.*, 2010, **10**, 1271–1275.
23 K. F. Mak, C. Lee, J. Hone, J. Shan and T. F. Heinz, *Phys. Rev. Lett.*, 2010, **105**, 136805.
24 H. S. Nalwa, *RSC Adv.*, 2020, **10**, 30529–30602.
25 F. Bonaccorso, Z. Sun, T. Hasan and A. C. Ferrari, *Nat. Photonics*, 2010, **4**, 611–622.
26 F. H. L. Koppens, T. Mueller, P. Avouris, A. C. Ferrari, M. S. Vitiello and M. Polini, *Nat. Nanotechnol.*, 2014, **9**, 780–793.
27 A. M. Shafi, F. Ahmed, H. A. Fernandez, M. G. Uddin, X. Cui, S. Das, Y. Dai, V. Khayrudinov, H. H. Yoon, L. Du, Z. Sun and H. Lipsanen, *ACS Appl. Mater. Interfaces*, 2022, **14**, 31140–31147.
28 J. F. Gonzalez Marin, D. Unuchek, K. Watanabe, T. Taniguchi and A. Kis, *npj 2D Mater. Appl.*, 2019, **3**, 14.
29 L. Tao, Z. Chen, Z. Li, J. Wang, X. Xu and J.-B. Xu, *InfoMat*, 2021, **3**, 36–60.
30 D. Hlushchenko, J. Olszewski, T. Martynkien, M. Łukomski, K. Gemza, P. Karasiński, M. ZiĘba, T. Baraniecki, Ł. Duda, A. Bachmatiuk, *et al.*, *ACS Appl. Mater. Interfaces*, 2024, **16**, 28874–28885.
31 Q. Li, J. Lu, P. Gupta and M. Qiu, *Adv. Opt. Mater.*, 2019, **7**, 1900595.
32 M. F. Khan, F. Ahmed, S. Rehman, I. Akhtar, M. A. Rehman, P. A. Shinde, K. Khan, D.-K. Kim, J. Eom, H. Lipsanen, *et al.*, *Nanoscale*, 2020, **12**, 21280–21290.
33 L. Huang, A. Krasnok, A. Alú, Y. Yu, D. Neshev and A. E. Miroshnichenko, *Rep. Prog. Phys.*, 2022, **85**, 046401.
34 J. S. Ross, S. Wu, H. Yu and W. Yao, *Nat. Commun.*, 2013, **4**, 1474.
35 F. Xia, T. Mueller, Y.-m. Lin, A. Valdes-Garcia and P. Avouris, *Nat. Nanotechnol.*, 2009, **4**, 839–843.
36 G. H. Shin, C. Park, K. J. Lee, H. J. Jin and S.-Y. Choi, *Nano Lett.*, 2020, **20**, 5741–5748.
37 Y. Venkata Subbaiah, K. Saji and A. Tiwari, *Adv. Funct. Mater.*, 2016, **26**, 2046–2069.
38 M. H. Tahersima and V. J. Sorger, *Nanotechnology*, 2015, **26**, 344005.
39 Q. Dong, X. Sun, L. Gao, Y. Zheng, R. Wu and Y. Cheng, *Nanomaterials*, 2025, **15**, 72.
40 S.-J. Tang, S. Liu, X.-C. Yu, Q. Song, Q. Gong and Y.-F. Xiao, *Adv. Mater.*, 2018, **30**, 1800262.
41 L. Huang, A. Krasnok, A. Alu, Y. Yu, D. Neshev and A. E. Miroshnichenko, *Rep. Prog. Phys.*, 2022, **85**, 046401.
42 T.-X. Huang, X. Cong, S.-S. Wu, K.-Q. Lin, X. Yao, Y.-H. He, J.-B. Wu, Y.-F. Bao, S.-C. Huang, X. Wang, *et al.*, *Nat. Commun.*, 2019, **10**, 5544.
43 H. Li, Q. Zhang, C. C. R. Yap, B. K. Tay, T. H. T. Edwin, A. Olivier and D. Baillargeat, *Adv. Funct. Mater.*, 2012, **22**, 1385–1390.
44 R. Hao, X. Li, L. Zhang, L. Zhang, H. You and J. Fang, *Nanoscale*, 2022, **14**, 10449–10455.
45 M. H. P. Pfeiffer, A. Kordts, V. Brasch, M. Zervas, M. Geiselmann, M. L. Gorodetsky and T. J. Kippenberg, *Optica*, 2016, **3**, 20–25.
46 D. Bose, M. W. Harrington, A. Isichenko, K. Liu, J. Wang, N. Chauhan, Z. L. Newman and D. J. Blumenthal, *Light: Sci. Appl.*, 2024, **13**, 156.
47 X. Gan, K. F. Mak, Y. Gao, Y. You, F. Hatami, J. Hone, T. F. Heinz and D. Englund, *Nano Lett.*, 2012, **12**, 5626–5631.
48 M. Engel, M. Steiner and P. Avouris, *Nat. Commun.*, 2012, **3**, 906.
49 N. Youngblood, C. Chen, S. J. Koester and M. Li, *Nat. Photonics*, 2015, **9**, 247–252.
50 F. Ahmed, M. S. Choi, X. Liu and W. J. Yoo, *Nanoscale*, 2015, **7**, 9222–9228.
51 A. Pospischil, M. M. Furchi and T. Mueller, *Nat. Nanotechnol.*, 2014, **9**, 257–261.
52 D. A. Bandurin, A. V. Tyurnina, G. L. Yu, A. Mishchenko, V. Zólyomi, S. V. Morozov, R. K. Kumar, R. V. Gorbachev, Z. R. Kudrynskyi, S. Pezzini, *et al.*, *Nat. Nanotechnol.*, 2017, **12**, 223–227.
53 Y. Liu, Y. Huang and X. Duan, *Nature*, 2019, **567**, 323–333.
54 X.-X. Wang, G. Zeng, Q.-J. Yu, L. Shen, C.-Y. Shi and H.-L. Lu, *Nanoscale*, 2024, **16**, 5504–5520.
55 D. Ahn, L. C. Kimerling and J. Michel, *J. Lightwave Technol.*, 2010, **28**, 3387–3394.
56 G. Wu, X. Wang, Y. Chen, Z. Wang, H. Shen, T. Lin, W. Hu, J. Wang, S. Zhang and X. Meng, *Nanotechnology*, 2018, **29**, 485204.
57 J. Miao, X. Liu, K. Jo, K. He, R. Saxena, B. Song, H. Zhang, J. He, M.-G. Han, W. Hu and D. Jariwala, *Nano Lett.*, 2020, **20**, 2907–2915.
58 M. Massicotte, P. Schmidt, F. Vialla, K. G. Schädler, A. Reserbat-Plantey, K. Watanabe, T. Taniguchi, K.-J. Tielrooij and F. H. L. Koppens, *Nat. Nanotechnol.*, 2016, **11**, 42–46.
59 N. Flöry, P. Ma, Y. Salamin, A. Emboras, T. Taniguchi, K. Watanabe, J. Leuthold and L. Novotny, *Nat. Nanotechnol.*, 2020, **15**, 118–124.
60 J. Wu, H. Ma, C. Zhong, M. Wei, C. Sun, Y. Ye, Y. Xu, B. Tang, Y. Luo, B. Sun, *et al.*, *Nano Lett.*, 2022, **22**, 6816–6824.
61 G. Y. Huang, Y. Hao, S. Q. Li, Y. D. Jia, J. C. Guo, H. Zhang and B. Wang, *J. Phys. D: Appl. Phys.*, 2023, **56**, 113001.
62 Y. J. Noori, Y. Cao, J. Roberts, C. Woodhead, R. Bernardo-Gavito, P. Tovee and R. J. Young, *ACS Photonics*, 2016, **3**, 2515–2520.
63 L. Stern, B. Desiatov, N. Mazurski and U. Levy, *Nat. Commun.*, 2017, **8**, 14461.
64 X. Zhang, M. Harrison, A. Harker and A. M. Armani, *Opt. Express*, 2012, **20**, 22298–22307.
65 Y. Ma, B. Dong, J. Wei, Y. Chang, L. Huang, K.-W. Ang, C. Lee, *et al.*, *Adv. Opt. Mater.*, 2020, **8**, 2000337.
66 H. Zhou, T. Gu, J. F. McMillan, M. Yu, G.-Q. Lo, D.-L. Kwong, G. Feng, S. Zhou and C. W. Wong, *Appl. Phys. Lett.*, 2016, **108**, 111106.
67 Y. Terada, K. Miyasaka, H. Ito and T. Baba, *Opt. Lett.*, 2016, **41**, 289–292.
68 O. Lopez-Sanchez, D. Lembke, M. Kayci, A. Radenovic and A. Kis, *Nat. Nanotechnol.*, 2013, **8**, 497–501.

69 M. Buscema, M. Barkelid, V. Zwiller, H. S. J. van der Zant, G. A. Steele and A. Castellanos-Gomez, *Nano Lett.*, 2013, **13**, 358–363.
70 S. Schuler, J. E. Muench, A. Ruocco, O. Balci, D. van Thourhout, V. Sorianello, M. Romagnoli, K. Watanabe, T. Taniguchi, I. Goykhman, A. C. Ferrari and T. Mueller, *Nat. Commun.*, 2021, **12**, 3733.
71 J. Guo, Z. Wu and Y. Zhao, *Opt. Express*, 2017, **25**, 10057–10069.
72 L. Tao, Z. Chen, Z. Li, J. Wang, X. Xu and J.-B. Xu, *InfoMat*, 2021, **3**, 36–60.
73 X. Gan, R.-J. Shiue, Y. Gao, S. Assefa, J. Hone and D. Englund, *IEEE J. Sel. Top. Quantum Electron.*, 2013, **20**, 95–105.
74 F. Xia, H. Wang, D. Xiao, M. Dubey and A. Ramasubramaniam, *Nat. Photonics*, 2014, **8**, 899–907.
75 K. Kinoshita, R. Moriya, M. Onodera, Y. Wakafuji, S. Masubuchi, K. Watanabe, T. Taniguchi and T. Machida, *npj 2D Mater. Appl.*, 2019, **3**, 22.